The Astrophysical Journal, 893:90 (15pp), 2020 April 20 https://doi.org/10.3847/1538-4357/ab8001

An XMM-Newton X-Ray View of Supernova Remnant W49B: Revisiting Its Recombining Plasmas and Progenitor Type

Lei Sun (孫磊)[1] and Yang Chen (陳陽)[1,2]
[1] Department of Astronomy, Nanjing University, Nanjing 210023, People's Republic of China
[2] Key Laboratory of Modern Astronomy and Astrophysics, Nanjing University, Ministry of Education, People's Republic of China; ygchen@nju.edu.cn
Received 2019 November 5; revised 2020 February 12; accepted 2020 March 12; published 2020 April 20

Abstract

We present a comprehensive X-ray spectroscopy and imaging study of supernova remnant W49B using archival XMM-Newton observations. The overionization state of the shocked ejecta in W49B is clearly indicated by the radiative recombination continua of Si XIV, S XV, and Fe XXV, combined with the Lyα lines of Ca and Fe. The line flux images of W49B indicate high emission measures of the central bar-like region for almost all of the emission lines, while the equivalent width maps reveal a stratified structure for the metal abundance distributions. The global spectrum of W49B is well reproduced by a model containing one collisional ionization equilibrium (CIE) plasma component and two recombining plasma (RP) components. The CIE plasma represents the shocked interstellar medium, which dominates the X-ray emitting volume in W49B with a mass $\sim$450 $M_{\odot}$. The two RP components with a total mass $\sim$4.6 $M_{\odot}$ are both dominated by the ejecta material, but characterized by different electron temperatures ($\sim$1.60 and $\sim$0.64 keV). The recombination ages of the RP components are estimated as $\sim$6000 yr and $\sim$3400 yr, respectively. We then reveal the possibility of a thermal conduction origin for the high-temperature RP in W49B by calculating the conduction timescale. The metal abundance ratios of the ejecta in W49B are roughly consistent with a core-collapse explosion model with a $\lesssim$15 $M_{\odot}$ progenitor, except for a rather high Mn/Fe. A Type Ia origin can explain the Mn abundance, while it predicts much higher ejecta masses than observed values for all of the metal species considered in our analysis.

Unified Astronomy Thesaurus concepts: Supernova remnants (1667); Interstellar medium (847); X-ray astronomy (1810)

1. Introduction

With the advances in X-ray imaging spectroscopy over the last two decades, substantial progress has been made in the study of supernova remnant (SNR) physics. Two of the major concerns have been intensively given to the evolution mechanism of SNR plasma and its implications for supernova (SN) physics.

1.1. Recombining Plasma

In the early phases of the SNR evolution, the ambient materials and the SN ejecta are compressed and heated by the forward and reverse shocks, respectively, leaving behind X-ray emitting plasmas. Due to the rather low density, the shock-heated plasma is expected to be in the nonequilibrium ionization (NEI) state for a long time. Most of the young or middle-aged SNRs are reported to involve ionizing (under-ionized) plasma (IP), where the ionization temperature (kT_z) is still lower than the electron temperature (kT_e). However, recent X-ray spectroscopic studies of several SNRs (e.g., IC 443, G359.1-0.5, W28, W44, etc.: Kawasaki et al. 2002; Yamaguchi et al. 2009; Ohnishi et al. 2011; Sawada & Koyama 2012; Uchida et al. 2012) revealed the existence of recombining (overionized) plasma (RP), where kT_z goes even higher than kT_e. So far, RP has been found in more than a dozen SNRs, which may represent a new subclass of SNRs.

The physical origin of the RPs observed in SNRs is still under debate. Theoretically, there are two possible ways to produce overionized plasma: increase of kT_z (extra ionization) or decrease of kT_e (electron cooling). The extra-ionization process can be caused by suprathermal electrons (e.g., Ohnishi et al. 2011) or high-energy photons (e.g., Kawasaki et al. 2002). On the other hand, the electron cooling scenario, which can better apply to the SNR evolution, may arise from adiabatic expansion (e.g., Itoh & Masai 1989) and/or thermal conduction (e.g., Kawasaki et al. 2002; Zhou et al. 2011). In addition, various scenarios (such as the adiabatic expansion and the thermal conduction scenario) may simultaneously contribute to the formation of RP, as indicated by Zhou et al. (2011) and Zhang et al. (2019) based on hydrodynamic simulations.

While the nature of RP remains unclear, spatially resolved X-ray spectroscopic studies of SNRs have provided us with significant clues. A higher degree of overionization (or a lower kT_e) toward the cold dense interstellar medium (ISM) may be indicative of a thermal conduction scenario (e.g., G166.0+4.2, CTB 1: Matsumura et al. 2017; Katsuragawa et al. 2018). In contrast, a higher degree of overionization toward low density regions may be indicative of an adiabatic expansion scenario (e.g., W49B: Miceli et al. 2010; Lopez et al. 2013; Yamaguchi et al. 2018). On the other hand, some common features shared by the RP-detected SNRs may give further implications. In Table 1 we summarize the basic information and the bulk RP properties of the 15 RP-detected Galactic SNRs. We note that most of the RP-detected SNRs (a) belong to the group of so-called thermal composite (or mixed-morphology) SNRs (Zhang et al. 2015), (b) are interacting with molecular clouds (Jiang et al. 2010), and (c) emit GeV/TeV γ-rays (Suzuki et al. 2018).

1.2. SN Progenitor

One of the most important issues regarding SNR science is the nature of their progenitors and their intrinsic properties. The shock-heated SN ejecta become luminous in the SNR phase, which can probe the progenitor type and the detailed explosion

Table 1
List of 15 RP-detected Galactic SNRs

Basic Information					Bulk RP Property					
Name	Age[a] (kyr)	MC Interaction[b]	GeV Emission[a]	Progenitor's Mass[c] ($M_\odot$)	Main Recombining Feature	Temperature kT_e (keV)	Ionization Parameter $n_e t$ (cm^{-3} s)	Metal Abundance[d]	Possible Origin of RP	Reference
G6.4−0.1 (W28)	33–36	Y, OH	Y		RRCs of He-like Si and S; Lyα lines of Mg and Si	LT: ∼0.1–0.2; HT: $\gtrsim$0.3	LT: $\sim 1 \times 10^{12}$; HT: $\sim(4–5) \times 10^{11}$	$\lesssim$	AE, TC	[1, 2, 3, 4]
G31.9+0.0 (3C 391)	7.4–8.4	Y, OH	Y	$\gtrsim$12	RRCs of H-like Si and S; Lyα lines of Si and S	∼0.5	$\sim 1.4 \times 10^{12}$	$\lesssim$	AE, TC	[5, 6]
G34.7−0.4 (W44)	7.9–8.9	Y, OH	Y	8–15 ?	RRCs of H-like Si and S; Lyα line of Si	∼0.4–0.5	$\sim(6–7) \times 10^{11}$	$\gtrsim$	AE	[7]
G43.3−0.2 (W49B)	2.9–6	Y ?	Y	$\gtrsim$13/∼25 /SN Ia ?	RRCs of H-like Si, He-like S, and He-like Fe; Lyα lines of Ca and Fe	LT: ∼0.64; HT: ∼1.6	LT: $\sim 5.5 \times 10^{11}$; HT: $\sim 3.9 \times 10^{11}$	>	AE, TC	This work; [8, 9, 10, 11, 12]
G53.6−2.2 (3C 400.2)	15–110		Y		RRCs of H-like O and Ne, and He-like Mg	∼0.06–0.15 /∼0.6–0.7 ?	$\sim(1–2) \times 10^{11}$	∼/>?	AE	[13, 14]
G89.0+4.7 (HB 21)	4.8–15	Y	Y		RRCs of H-like Si and S	∼0.17	$\sim 3.2 \times 10^{11}$	>		[15]
G116.9+0.2 (CTB 1)	7.5–15			$\gtrsim$13	RRCs of H- and He-like Ne	∼0.15–0.20	$\sim(7–10.5) \times 10^{11}$	$\gtrsim$	TC	[16]
G160.9+2.6 (HB 9)	4–7	?	Y			∼1.13	$\sim 5.8 \times 10^{11}$	$\gtrsim$	AE	[17]
G166.0+4.3 (VRO 42.05.01)		?	Y		RRC of He-like Si; Lyα lines of Si and S	∼0.46	$\sim 6.1 \times 10^{11}$	$\lesssim$	TC	[18]
G189.1+3.0 (IC 443)	3–30	Y, OH	Y	$\gtrsim$15	Heα lines of Fe and Ni; Lyα lines of Si, S, Ar, Ca and Fe; RRCs of He-like Fe and H-like Mg, Si, S and Ca	LT: ∼0.16–0.28; HT: ∼0.48–0.67	$\sim 5 \times 10^{11}$	$\gtrsim$	AE, TC	[19, 20, 21, 22, 23]
G290.1−0.8 (MSH 11-61A)	10–20	?	Y	25–30	Lyα line of Si; RRC of H-like Si	∼0.3–0.5	$\sim 1 \times 10^{12}$	>	AE	[24, 25]
G304.6+0.1 (Kes 17)	2–64	Y	Y		Lyα lines of Si and S; RRC of H-like Si	∼0.6–0.7	$\sim(1.1–1.6) \times 10^{12}$	$\gtrsim$	TC	[26]
G346.6−0.2	4.2–16	Y, OH			RRCs of He-like Si and S	∼0.2–0.3	$\sim(4–6) \times 10^{11}$	$\lesssim$	AE	[27, 28]
G348.5+0.1 (CTB 37A)	10–30	Y, OH	Y		RRCs of He-like Mg and Si	∼0.5	$\sim 1.3 \times 10^{12}$	$\gtrsim$		[29]
G359.1−0.5	>10	Y, OH	Y		Lyα lines of Si and S; RRCs of He-like Si and S	∼0.29		>		[30]

Notes. "Y" in the table stands for yes; "?" means that the property is uncertain or controversial; "LT" and "HT" refer to low-temperature and high-temperature components, respectively; and "AE" and "TC" stand for adiabatic expansion and thermal conduction, respectively.

[a] Adopted from the catalog of high-energy observations of Galactic SNRs (Ferrand & Safi-Harb 2012s; also see http://www.physics.umanitoba.ca/snr/SNRcat/ for the latest online version).

[b] Adopted from the SNR–MC association table in Jiang et al. (2010); "OH" means that the 1720 MHz OH maser is detected.

[c] Adopted from the thermal composite SNR table in Zhang et al. (2015).

[d] Compare with 1 solar abundance.

References. [1] Sawada & Koyama (2012), [2] Zhou et al. (2014), [3] Pannuti et al. (2017), [4] Okon et al. (2018), [5] Ergin et al. (2014), [6] Sato et al. (2014), [7] Uchida et al. (2012), [8] Ozawa et al. (2009), [9] Miceli et al. (2010), [10] Lopez et al. (2013), [11] Zhou & Vink (2018), [12] Yamaguchi et al. (2018), [13] Broersen & Vink (2015), [14] Ergin et al. (2017), [15] Suzuki et al. (2018), [16] Katsuragawa et al. (2018), [17] Sezer et al. (2019), [18] Matsumura et al. (2017), [19] Kawasaki et al. (2002), [20] Yamaguchi et al. (2009), [21] Ohnishi et al. (2014), [22] Matsumura et al. (2017), [23] Greco et al. (2018), [24] Kamitsukasa et al. (2015), [25] Auchettl et al. (2015), [26] Washino et al. (2016), [27] Yamauchi et al. (2013), [28] Auchettl et al. (2017), [29] Yamauchi et al. (2014), [30] Ohnishi et al. (2011).

Table 2
Observations

ObsID	Date	t_{exp} (ks)[a]			∑ GTI (ks)[b]		
		MOS1	MOS2	pn	MOS1	MOS2	pn
0084100401	2004 Apr 3	18.7	18.7	17.0	17.0	16.9	14.6
0084100501	2004 Apr 5	18.7	18.7	17.0	17.6	16.6	15.1
0084100601[c]	2004 Apr 13	2.6	2.5	…	…	…	…
0724270101	2014 Apr 18	117.2	117.1	115.5	105.6	110.2	71.0
0724270201	2014 Apr 19	69.9	69.8	68.3	33.8	38.9	16.8
Total		227.1	226.8	217.8	174.0	182.6	117.5

Notes.
[a] Total exposure times.
[b] Total GTIs after SP flare removal.
[c] Observation is heavily contaminated by SP flares.

mechanism. Meanwhile, the shocked circumstellar material (CSM) can help to trace the history of the progenitor evolution up to thousands and even millions of years before the explosion (see, e.g., Patnaude & Badenes 2017 for a recent review). However, identification of the progenitor and explosion type for individual SNRs remains a major challenge in SNR studies.

Thermonuclear (Type Ia) SNe typically produce a large amount of iron group elements (IGEs) such as Fe and Ni, while core-collapse (CC) SNe usually result in high yields of O, Ne, and Mg. Therefore, metal abundances of the ejecta material are commonly used as indicators of the progenitor type. Particularly, detailed analyses on the abundance ratios of different metal species may help to disentangle the ejecta from the CSM, and provide further constraints on the progenitor (e.g., Sun & Chen 2019). Moreover, the progenitor type can also be identified based on the bulk properties of SNRs. The Fe K line centroids detected in Type Ia SNRs have been found to be generally lower than those detected in CC SNRs, which may be a useful diagnostic to discriminate the SNR type (Yamaguchi et al. 2014; Patnaude et al. 2015). In addition, Yang et al. (2013) proposed the Cr-to-Fe equivalent width (EW) ratio ($\gamma_{Cr/Fe} \equiv EW_{Cr}/EW_{Fe}$) as a discriminant of the progenitor type. On the other hand, the X-ray morphology of the SNRs can also be used to constrain their progenitor types (Lopez et al. 2009, 2011).

1.3. SNR W49B

SNR W49B is one of the most intriguing objects in SNR science. It is a mixed-morphology SNR (Rho & Petre 1998) at a distance of 8–11.3 kpc (e.g., Radhakrishnan et al. 1972; Moffett & Reynolds 1994; Chen et al. 2014; Zhu et al. 2014; Ranasinghe & Leahy 2018), and is among the most luminous Galactic SNRs in 1 GHz radio band, Fe K line X-rays, and GeV γ-rays (e.g., Moffett & Reynolds 1994; Yamaguchi et al. 2014; H.E.S.S. Collaboration et al. 2018). W49B is suggested to originate inside a wind-blown bubble interior to a dense molecular cloud (Keohane et al. 2007). The CO observations further reveal the evolution of the SNR in a molecular cavity at a distance of 9.3 kpc (Chen et al. 2014; Zhu et al. 2014).

W49B is one of the first RP-detected SNRs (Kawasaki et al. 2005; Ozawa et al. 2009), represented by the remarkable radiative recombining continuum (RRC) of He-like Fe. The physical origin of the RP is not fully understood. Spatially resolved X-ray studies have shown that the distribution of the RP is most consistent with the adiabatic cooling scenario (Miceli et al. 2010; Lopez et al. 2013; Yamaguchi et al. 2018), while the thermal conduction between plasma and ambient cold clouds could also be important based on hydrodynamic simulations (Zhou et al. 2011; Zhang et al. 2019). Notably, W49B might be the youngest one (1000–6000 yr, e.g., Pye et al. 1984; Smith et al. 1985; Hwang et al. 2000; Zhou & Vink 2018) and the only one that originates from SN Ia (Zhou & Vink 2018) among the RP-detected SNRs (see Table 1).

However, the progenitor SN type of W49B is a perplexing question which has been debated for a long time. It is usually considered as a CC SNR, given its peculiar morphology and ambient environment (e.g., Miceli et al. 2006; Keohane et al. 2007). Moreover, it has been suggested that W49B comes from a jet-driven Type Ib/Ic explosion, and might be the first candidate of its kind that harbors a newborn black hole (Lopez et al. 2013). However, recent studies on the X-ray spectrum of W49B have shown that the metal abundances of the ejecta are better described by SN Ia models (Zhou & Vink 2018).

Aiming at a new insight of the relevant physics of W49B, we present an analysis of the archival XMM-Newton data of the SNR. The paper is organized as follows: Section 2 describes the observation data and the reduction procedure; Section 3 presents the main results, in terms of the global spectra (Section 3.1) and the imaging analysis (Section 3.2); Section 4 discusses the results, mainly focusing on the new constraints of the RP properties and the SN progenitor; and finally, Section 5 gives a brief summary. The errors quoted in this paper represent 90% confidence ranges unless otherwise stated.

2. Observations and Data Reduction

SNR W49B was observed with XMM-Newton EPIC-MOS and EPIC-pn cameras in 2004 (PI: A. Decourchelle) and 2014 (PI: L. A. Lopez). We reduce the data based on XMM-Newton Science Analysis Software (SAS, version 16.1.0).[3] All the observation data files are reprocessed using SAS tasks `emchain` and `epchain`. Then, `mos-filter` and `pn-filter` are used to filter out soft proton (SP) flares and to remove affected time intervals. The observation with ObsID 0084100601 is heavily contaminated by SP flares, and thus is excluded from our analysis. The total good time intervals (GTIs) after SP flare removal are 174.0 ks, 182.6 ks, and 117.5 ks for the MOS1, MOS2, and pn data, respectively, as summarized in Table 2.

[3] https://www.cosmos.esa.int/web/xmm-newton/sas

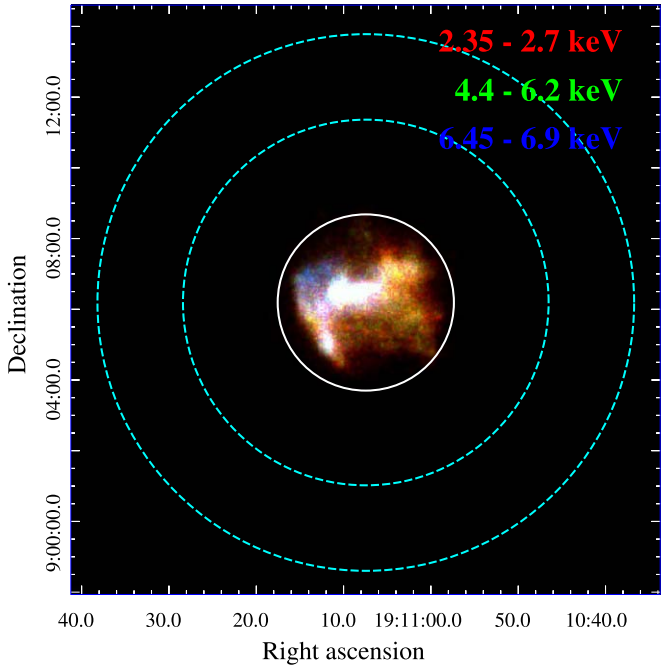

Figure 1. Merged image of the XMM-Newton EPIC observations of W49B. Red: 2.35–2.7 keV (S Heα and Lyα); green: 4.4–6.2 keV (continuum); blue: 6.45–6.9 keV (Fe K complex). The white solid circle indicates the region for global spectra extraction and the cyan dashed annulus indicates the region for background spectra extraction.

We use SAS tasks `mos-spectra` and `pn-spectra` to create the images and spectra of a given region in a certain energy band. Meanwhile, `mos_back` and `pn_back` are used to estimate the quiescent particle background (QPB). For image analysis, we adopt tasks `merge_comp_xmm` to produce the combined count images, exposure maps, and QPB images of all the observations. We use `adapt_merge` to adaptively smooth the QPB-subtracted and vignetting-corrected count images. All the spectra are grouped with a minimum of 25 counts per channel using FTOOLS task `grppha`. XSPEC (version 12.10.1)[4] with AtomDB 3.0.9[5] is used for spectral analysis.

3. X-Ray Properties

Figure 1 shows the merged XMM-Newton EPIC image of W49B, with red for 2.35–2.7 keV (including primarily the S Heα and S Lyα), green for 4.4–6.2 keV (the continuum), and blue for 6.45–6.9 keV (the Fe K complex).

3.1. Global Spectra

We extract the global spectra of W49B from a circular region that covers the whole SNR (as indicated by the white circle in Figure 1). The spectra are shown in Figure 2, and are dominated by emission lines from the He-like and H-like ions of Si, S, Ar, and Ca, and by an intense Fe K line complex. Lopez et al. (2013) reported a dramatic decline of the emission line fluxes for W49B during an 11 yr interval between two of the Chandra ACIS observations ($\sim$18% for Si XIII and $\lesssim$5% for other emission lines, from 2000 to 2011). However, it is difficult to figure out a proper astrophysical explanation for this line flux decrement. The XMM-Newton spectra of W49B extracted from 2004 and 2014 observations are consistent with each other and show no signs of line flux decrement (see Figure 2). We infer that a part of the flux decline indicated by Chandra observations may be caused by the quantum efficiency (QE) contamination of ACIS.[6] On the other hand, we find that there are some slight differences between the MOS spectra and the pn spectra (mainly in the $\lesssim$1.0 keV and $\gtrsim$7.0 keV energy bands). This may be caused by the different instrumental backgrounds of the two cameras (see, e.g., Katayama et al. 2004; Kuntz & Snowden 2008). In view of a simpler background and a better spectral resolution of the MOS camera, we use only the MOS spectra for our further spectral analysis.

For background analysis, we extract the spectra from an annulus region around the SNR (indicated by the dashed cyan circles in Figure 1). We jointly fit the 0.3–10.0 keV spectra using a background model that contains both the astrophysical and instrumental components. Following Masui et al. (2009) and Uchiyama et al. (2013), the astrophysical part of the background model consists of three components: a `powerlaw` model for the cosmic X-ray background (CXB), and two `apec` thin thermal plasma models for the foreground emission from the local hot bubble (LHB) and the Galactic emission (diffuse X-ray emission from the Galactic halo and the Galactic ridge), respectively. The CXB and the Galactic emission are subject to absorptions that are modeled with `phabs` code. The instrumental background mainly consists of two fluorescence lines: Al Kα $\sim$ 1.49 keV and Si Kα $\sim$ 1.74 keV (Kuntz & Snowden 2008). Another `powerlaw` component is included to account for the remaining SP contamination. All the parameters of the astrophysical components are linked between different observations, while the fluxes of the instrumental lines and the SP contamination are not, as they vary with detectors and observations. The model described above can basically reproduce the background spectra, but leaves a line-like residual at $\sim$6.7 keV and a narrow bump-like residual at $\sim$0.9 keV. The former feature is likely the Fe K emission from the high-temperature plasma in the Galactic ridge (Uchiyama et al. 2013). But the physical origin of the narrow bump-like structure is unclear. A similar feature has been noticed by Masui et al. (2009) based on a Suzaku observation of the Galactic plane, and they attributed it to the emission from unresolved dM stars. To keep the background model simple, we just add Gaussian components for these two features, and leave out further discussions on the detailed physical origins. Therefore, the background model can be finally described as:

$$\begin{aligned} &\mathtt{apec}_{\rm LHB} + \mathtt{phabs1} \times \mathtt{apec}_{\rm Gal} \\ &\quad + \mathtt{phabs2} \times \mathtt{powerlaw}_{\rm CXB} + \mathtt{powerlaw}_{\rm SP} \\ &\quad + \textstyle\sum_i \mathtt{gauss}_i, \end{aligned} \tag{1}$$

where $i = 1, 2, 3, 4$ denote the two instrumental lines (Al Kα $\sim$ 1.49 keV and Si Kα $\sim$ 1.74 keV) and the two

[4] https://heasarc.gsfc.nasa.gov/xanadu/xspec/
[5] http://www.atomdb.org/

[6] The effective ACIS QE is lower than it was at launch, and is continuously decreasing. As a reference, the effective area of ACIS-S at $\sim$1.8 keV (Si XIII band) was $\sim$640 cm^2 in 2000, while it declined to $\sim$610 cm^2 in 2011 (decreased by $\sim$5%). This QE contamination takes place mainly in the low-energy band, which may be responsible for a larger decrement of Si XIII flux than that of other emission lines. However, a decrement of $\sim$18% in line flux is still confusing. Further diagnosis of the Chandra data with the newest calibration is needed, which is, however, beyond the purpose of this work. For a comprehensive analysis of ACIS QE contamination, please refer to http://cxc.harvard.edu/ciao/why/acisqecontamN0010.html and the references therein.

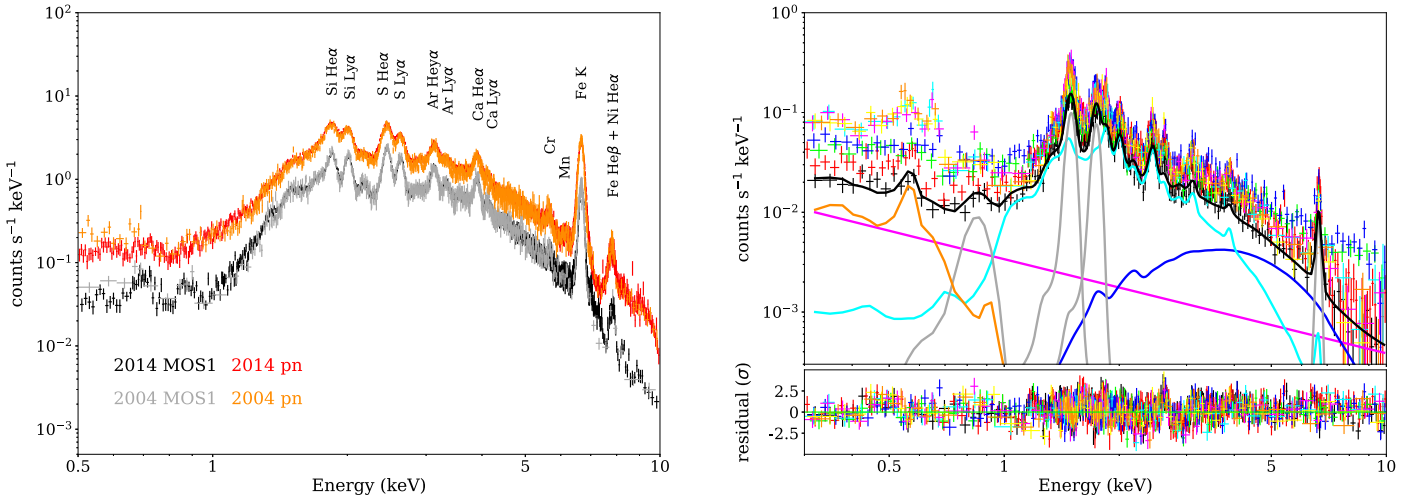

Figure 2. Left: a comparison between the global spectra of W49B taken in 2014 and those taken in 2004. The spectra are extracted from the region indicated by the white circle in Figure 1. Right: the background spectra (data points), with the best-fit model (solid curves, different colors for different components: CXB, LHB, Galactic emission, SP contamination, and the Gaussian components, are plotted in blue, orange, cyan, magenta, and gray, respectively) and residuals. The spectra are extracted from the region indicated by the cyan dashed annulus in Figure 1.

line-like features at ∼0.9 keV and ∼6.7 keV, respectively. The best-fit parameters are summarized in Table 3, and the fitted spectra are shown in Figure 2. The best-fit background model obtained here is then scaled by the area factors and used in the subsequent analysis of the source spectra.

Previous studies have shown that the spectrum of W49B can be well reproduced by a two-component model that contains a low-temperature plasma with solar abundance and a high-temperature plasma with super-solar abundance, representing the shocked ISM and ejecta, respectively (e.g., Hwang et al. 2000; Miceli et al. 2006; Lopez et al. 2013; Zhou & Vink 2018). Moreover, the shocked ISM is suggested to be under the collisional ionization equilibrium (CIE), while the shocked ejecta is found to have some overionization features, such as the RRC of Fe and high H-like to He-like line ratios of S, Ar, and Fe (e.g., Ozawa et al. 2009; Miceli et al. 2010; Lopez et al. 2013; Yamaguchi et al. 2018).

We start our spectral analysis by fitting the 0.5–10.0 keV global spectra of W49B with a simple two-temperature CIE model, and seeing whether additional components are needed.[7] The model, as shown in Figure 3(a), contains two absorbed `vvapec` components: one with solar abundances accounts for the ISM-dominated plasma, and the other with enhanced abundances accounts for the ejecta-dominated plasma. We find that this "2 CIE" model cannot properly reproduce the spectra and gives a large χ^2/dof ∼ 1.903(16069/8446). The most significant residual turns up around He-like Si and S lines and H-like Ar and Ca lines, which indicates other temperature components may be needed. We then try a "3 CIE" model by adding a third `vvapec` component for the ejecta-dominated plasma (Figure 3(b)). The fitting gets some improvements and χ^2/dof is reduced to ∼1.775(14987/8443). However, much of the residual in energies $\gtrsim$2.0 keV still exist. Adding a further plasma component cannot improve the fitting anymore. By carefully checking the residual, we find some signs for overionization, including (1) bump-like features at ∼3.2 and ∼8.8 keV, which may correspond to the RRCs of He-like S and He-like Fe, respectively (as well as a less significant feature at ∼2.7 keV which may related to the RRC of H-like Si); (2) emission-line-like features at ∼4.1 and ∼7.0 keV, which appear to correspond to Lyα lines of Ca and Fe. To further confirm these features, we add three `redge` components (for RRCs) and two `Gauss` components (for Lyα lines) to the model (Figure 3(c)). It gives acceptable fitting results and further reduces the χ^2/dof to ∼1.393(11750/8436). The fluxes of individual components are obtained as (in units of 10^{-4} photons s^{-1} cm^{-2}) $6.70^{+0.33}_{-0.17}$ for Si XIV RRC, $5.50^{+0.13}_{-0.16}$ for S XV RRC, $1.08^{+0.20}_{-0.16}$ for Fe XXV RRC, 0.51 ± 0.04 for Ca Lyα, and 0.22 ± 0.02 for Fe Lyα. Moreover, we get a temperature 0.64 ± 0.01 keV for the Si and S RRC, but a much higher temperature $1.08^{+0.20}_{-0.16}$ keV for the Fe RRC. It should be noted that the spectrum model here is just quasi-physical (CIE + overionization features), the fluxes and temperatures obtained above may differ from reality. However, it still

Table 3
Background Spectral Fitting Results

Parameter	Best-fit
LHB	
kT_e (keV)	0.15 ± 0.01
Norm[a] (10^{-5} cm^{-5})	$6.48^{+1.59}_{-0.71}$
Galactic X-Ray Emission	
N_H (10^{22} cm^{-2})	3.65 ± 0.04
kT_e (keV)	$1.12^{+0.01}_{-0.02}$
Norm[a] (10^{-3} cm^{-5})	$5.66^{+0.08}_{-0.19}$
CXB	
N_H (10^{22} cm^{-2})	=phabs1 × 2
α	1.4 (fixed)
Norm (10^{-4} photons s^{-1} cm^{-2} keV^{-1} at 1 keV)	1.54 ± 0.07
χ^2/ dof	1.18 (3378/2871)

Note.
[a] Defined as $10^{-14}/(4\pi d^2)\int n_e n_H dV$.

[7] Zhou & Vink (2018) reported the detection of several point-like sources in the W49B based on Chandra observations. Their overall flux is $\lesssim 10^{-5}$ photons s^{-1} cm^{-2} (0.7–5.0 keV), which is about three orders of magnitude lower than the flux of W49B. Thus the effects of the unresolved point-like sources can be ignored in our spectral fitting.

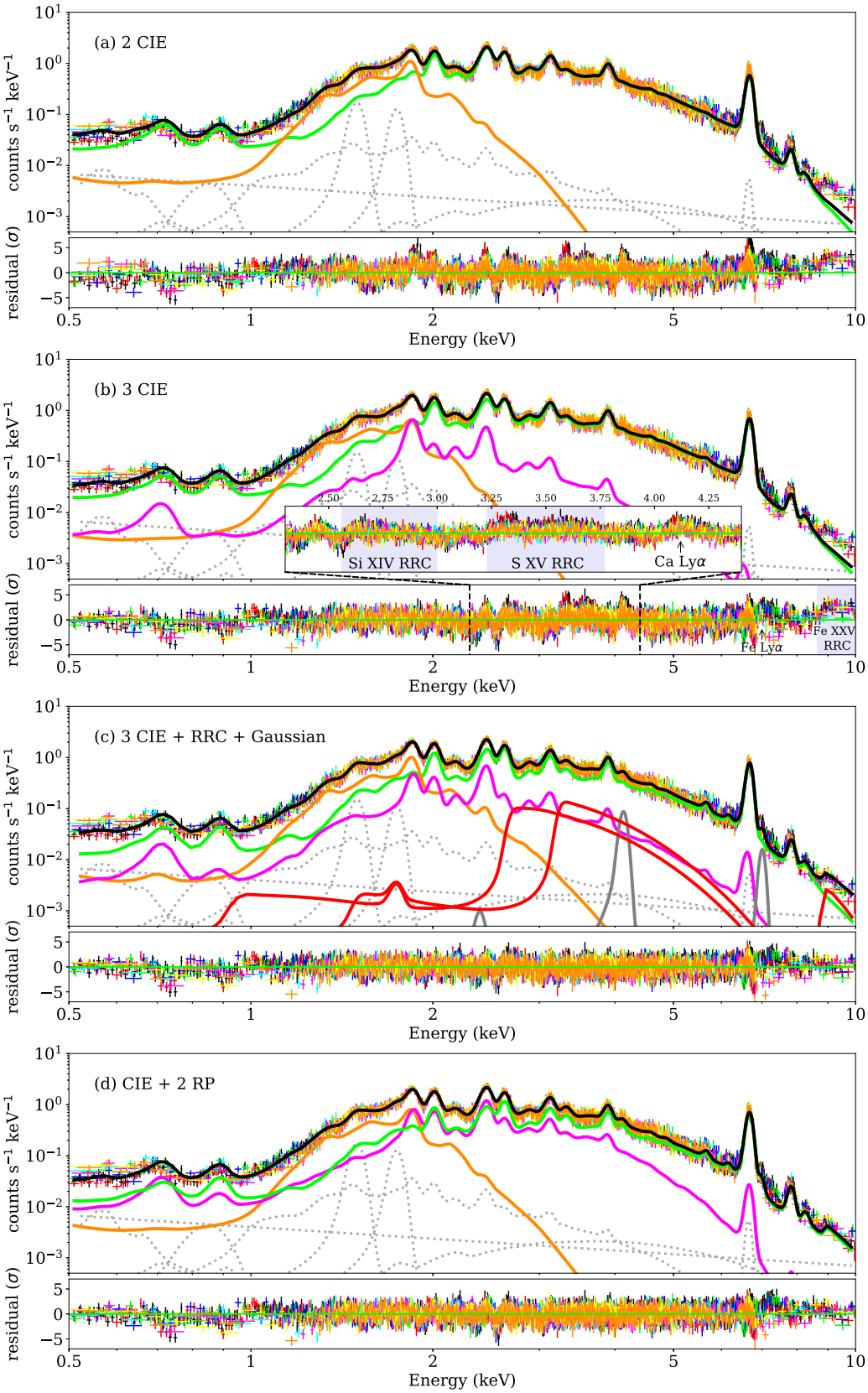

Figure 3. Global spectra of W49B (data points), with various spectral fit models (solid curves, different colors for different components) and residuals. Background components are plotted with light gray dotted curves. (a) "2 CIE" model, in which the orange curve denotes the ISM component and the green curve denotes the ejecta component; (b) "3 CIE" model, in which the magenta curve denotes the additional low-temperature ejecta component; (c) "3 CIE + RRC + Gaussian" model, in which RRCs are plotted in red and Lyα lines are plotted in dark gray; (d) "CIE + 2 RP" model, in which the high- and low-temperature RP components are plotted in green and magenta, respectively.

Table 4
Spectral Fitting Results for Global Spectra of W49B

Parameter	2 CIE	3 CIE	3 CIE + RRC + Gaussian	CIE + 2 RP
Absorption				
$N_{\rm H}$ (10^{22} cm^{-2})	$8.25^{+0.04}_{-0.03}$	7.84 ± 0.01	7.37 ± 0.01	8.26 ± 0.01
ISM				
$kT_{\rm e}$ (keV)	0.187 ± 0.001	0.174 ± 0.001	0.228 ± 0.001	0.177 ± 0.001
Mg	0.30 ± 0.02	0.26 ± 0.02	0.31 ± 0.02	0.31 ± 0.02
Norm[a] (cm^{-5})	$61.0^{+1.7}_{-1.4}$	$74.0^{+0.7}_{-0.6}$	$11.0^{+0.1}_{-0.2}$	$86.7^{+0.6}_{-0.7}$
Ejecta1				
$kT_{\rm e}$ (keV)	1.65 ± 0.01	1.82 ± 0.01	$1.90^{+0.02}_{-0.01}$	$1.60^{+0.02}_{-0.01}$
$kT_{\rm init}$ (keV)	...	...	...	$4.54^{+0.17}_{-0.07}$
Si	4.25 ± 0.05	4.36 ± 0.04	$6.05^{+0.05}_{-0.07}$	$7.61^{+0.08}_{-0.07}$
S	$4.48^{+0.04}_{-0.03}$	$4.51^{+0.03}_{-0.04}$	$7.50^{+0.05}_{-0.06}$	$10.39^{+0.07}_{-0.09}$
Ar	3.90 ± 0.07	$4.27^{+0.07}_{-0.08}$	$6.21^{+0.13}_{-0.11}$	$11.46^{+0.21}_{-0.18}$
Ca	4.12 ± 0.07	4.28 ± 0.07	6.37 ± 0.11	$11.63^{+0.21}_{-0.17}$
Cr	3.40 ± 0.47	$2.43^{+0.47}_{-0.42}$	$8.90^{+0.69}_{-0.68}$	$13.48^{+1.02}_{-1.08}$
Mn	$2.81^{+1.02}_{-1.01}$	<1.52	$10.53^{+1.43}_{-1.44}$	$19.40^{+2.10}_{-2.22}$
Fe	4.99 ± 0.04	$4.50^{+0.04}_{-0.03}$	7.13 ± 0.06	$10.24^{+0.07}_{-0.11}$
$n_e t$ (10^{11} cm^{-3} s)	...	...	...	$3.90^{+0.08}_{-0.04}$
Redshift (10^{-3})	$-2.81^{+0.02}_{-0.01}$	-2.79 ± 0.01	$-2.78^{+0.01}_{-0.02}$	-2.79 ± 0.01
Norm[a] (10^{-2} cm^{-5})	$14.52^{+0.13}_{-0.15}$	$11.96^{+0.12}_{-0.03}$	$6.64^{+0.01}_{-0.26}$	$5.63^{+0.04}_{-0.02}$
Ejecta2				
$kT_{\rm e}$ (keV)	...	0.73 ± 0.01	$1.02^{+0.01}_{-0.02}$	0.64 ± 0.01
$kT_{\rm init}$ (keV)	...	...	...	$2.42^{+0.05}_{-0.03}$
Abundance	...	=ejecta1	=ejecta1	=ejecta1
$n_e t$ (10^{11} cm^{-3} s)	...	...	...	$5.49^{+0.04}_{-0.09}$
Redshift (10^{-3})	...	$-0.28^{+0.10}_{-0.38}$	$-1.46^{+0.08}_{-0.11}$	$-3.74^{+0.04}_{-0.19}$
Norm[a] (10^{-2} cm^{-5})	...	$5.31^{+0.09}_{-0.10}$	$2.51^{+0.12}_{-0.05}$	$10.23^{+0.10}_{-0.07}$
RRC				
Si XIV Recombining Edge (keV)	...	...	2.67[b]	...
$kT_{\rm e}$ (keV)	...	...	0.64 ± 0.01	...
Norm (10^{-4} photons s^{-1} cm^{-2})	...	...	$6.70^{+0.33}_{-0.17}$	...
S XV Recombining Edge (keV)	...	...	3.22[b]	...
$kT_{\rm e}$ (keV)	...	...	=Si XIV	...
Norm (10^{-4} photons s^{-1} cm^{-2})	...	...	$5.50^{+0.13}_{-0.16}$	...
Fe XXV Recombining Edge (keV)	...	...	8.83[b]	...
$kT_{\rm e}$ (keV)	...	...	$1.08^{+0.20}_{-0.16}$	...
Norm (10^{-4} photons s^{-1} cm^{-2})	...	...	0.84 ± 0.09	...
Gaussian				
Ca Lyα Center (keV)	...	...	4.10[b]	...
Norm (10^{-4} photons s^{-1} cm^{-2})	...	...	0.51 ± 0.04	...
Fe Lyα Center (keV)	...	...	7.00[b]	...
Norm (10^{-4} photons s^{-1} cm^{-2})	...	...	0.22 ± 0.02	...
χ^2/dof	1.903(16069/8446)	1.775(14987/8443)	1.393(11750/8436)	1.396(11784/8439)

Notes.
[a] Defined as $10^{-14}/(4\pi d^2)\int n_{\rm e} n_{\rm H} dV$.
[b] Fixed value.

provides strong evidence of the overionization state not only for the Fe-rich ejecta, but also for the Si-, S-, and Ca-rich ejecta. Furthermore, it indicates a multitemperature composition of the RP.

In view of the analysis above, we construct a "CIE + 2 RP" model to finally fit the global spectra, in which the RP components are described by two `vvrnei` models embedded in XSPEC. The `vvrnei` model characterizes the spectrum of an NEI plasma, which is assumed to have started in collisional equilibrium with an initial temperature $kT_{\rm init}$ and is rapidly heated or cooled to a temperature $kT_{\rm e}$. This "CIE + 2 RP" model well reproduces the spectra with a χ^2/dof $\sim 1.396(11784/8439)$. The detailed parameter setting and the best-fit results are summarized in Table 4, and the fitted spectra are shown in Figure 3(d). Based on the results, the ejecta-dominated plasma in W49B has two major components with different thermal and ionization states.

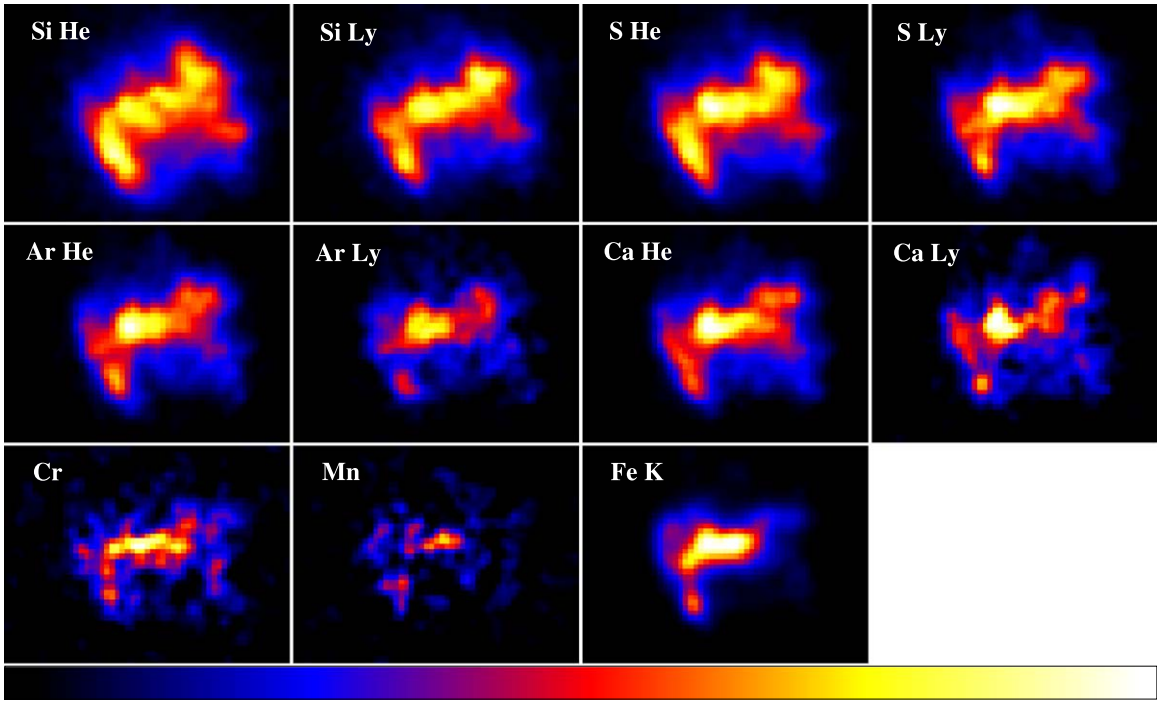

Figure 4. Vignetting-corrected, QPB- and continuum-subtracted images of line fluxes. The flux range between 0 and 70 (Si He), 60 (Si Ly), 100 (S He), 70 (S Ly), 70 (Ar He), 30 (Ar Ly), 60 (Ca He), 20 (Ca Ly), 6 (Cr), 5 (Mn), and 180 (Fe K), in units of counts s^{-1} deg^{-2}. The color bar has a linear scale.

Both of the components are overionized, and the current and initial electron temperatures are $kT_{e,1} = 1.60^{+0.02}_{-0.01}$ keV, $kT_{e,2} = 0.64 \pm 0.01$ keV and $kT_{init,1} = 4.54^{+0.17}_{-0.07}$ keV, $kT_{init,2} = 2.42^{+0.05}_{-0.03}$ keV, respectively. The ionization parameters are $n_{e,1}t_1 = 3.90^{+0.08}_{-0.04} \times 10^{11}$ and $n_{e,2}t_2 = 5.49^{+0.04}_{-0.09} \times 10^{11}$ cm^{-3} s.

3.2. EW Map

EW map is a powerful tool to investigate the spatial distribution of the true line strength while avoiding the contamination of the underlying continuum (e.g., Hwang et al. 2000). Miceli et al. (2006) produced EW maps of S, Ar, Ca, and Fe for W49B based on the ~30 ks XMM-Newton data (i.e., the first two observations listed in Table 2). However, their results were limited by the exposure time and total net counts. The additional ~150 ks observations can help us carry out EW analysis with much more detail.

To define the energy ranges for individual emission lines, we carefully analyze the 1.5–7.0 keV spectra by fitting them with a phenomenological model that consists of two thermal bremsstrahlung continua and several Gaussian lines. We obtain the energy ranges for all the Heα and Lyα lines of Si, S, Ar, and Ca, for Heα lines of Cr and Mn, and for Fe K complex (as summarized in Table 5). For each emission line, we select a low-energy continuum C_{low} and a high-energy continuum C_{high}, and use a linear interpolation (or extrapolation) between them to estimate the underlying continuum. The true line flux is obtained by subtracting the underlying continuum. Then, the EW can be calculated as the ratio between the truly line flux and the continuum flux density at the line centroid. It should be noted that the continuum-subtracted line flux represents the emission measure of a certain ion, which is proportional not only to the ion density but also to the electron density and the emission volume. On the other hand, the EW is linearly related to the abundance but is still affected by the temperature and the ionization state.

Table 5
Energy Bands Used to Construct EW Maps

	Line (eV)	C_{low} (eV)	C_{high} (eV)
Si Heα	1770–1930	1500–1600	2750–2830
Si Lyα	1930–2090	1500–1600	2750–2830
S Heα	2350–2550	1500–1600	2750–2830
S Lyα	2550–2710	1500–1600	2750–2830
Ar Heα	3020–3240	2750–2830	3450–3550
Ar Lyα	3240–3400	2750–2830	3450–3550
Ca Heα	3770–4020	3450–3550	4300–4450
Ca Lyα	4020–4220	3450–3550	4300–4450
Cr	5560–5760	5250–5450	5850–6000
Mn	6090–6260	5250–5450	5850–6000
Fe K	6420–6920	5250–5450	5850–6000

The vignetting-corrected, QPB- and continuum-subtracted images of line fluxes are shown in Figure 4. The EW maps are shown in Figure 5. The images are produced using the SAS task `adapt_merge`, which rebins the images to a pixel size of $0.''12 \times 0.''12$ and adaptively smooths the images with a minimum count of 25. Similar to Miceli et al. (2006), we find a bright central bar-like structure in all the line flux images, which is also the most luminous part of W49B in X-rays. The line fluxes of intermediate mass elements (IMEs) such as Si, S, Ar, and Ca show similar distributions with bright knots present at both sides of the central bar. Fe K complex has a peculiar distribution concentrated in the northeast part of the remnant while it is almost unseen in the southwest. Mn shows a similar distribution to Fe K. On the other hand, EW maps reveal unique properties that are quite different from the line fluxes. A central-bright pattern is only preserved in the EW maps of Fe K and Mn, while for the IMEs, high EWs appear mainly on the

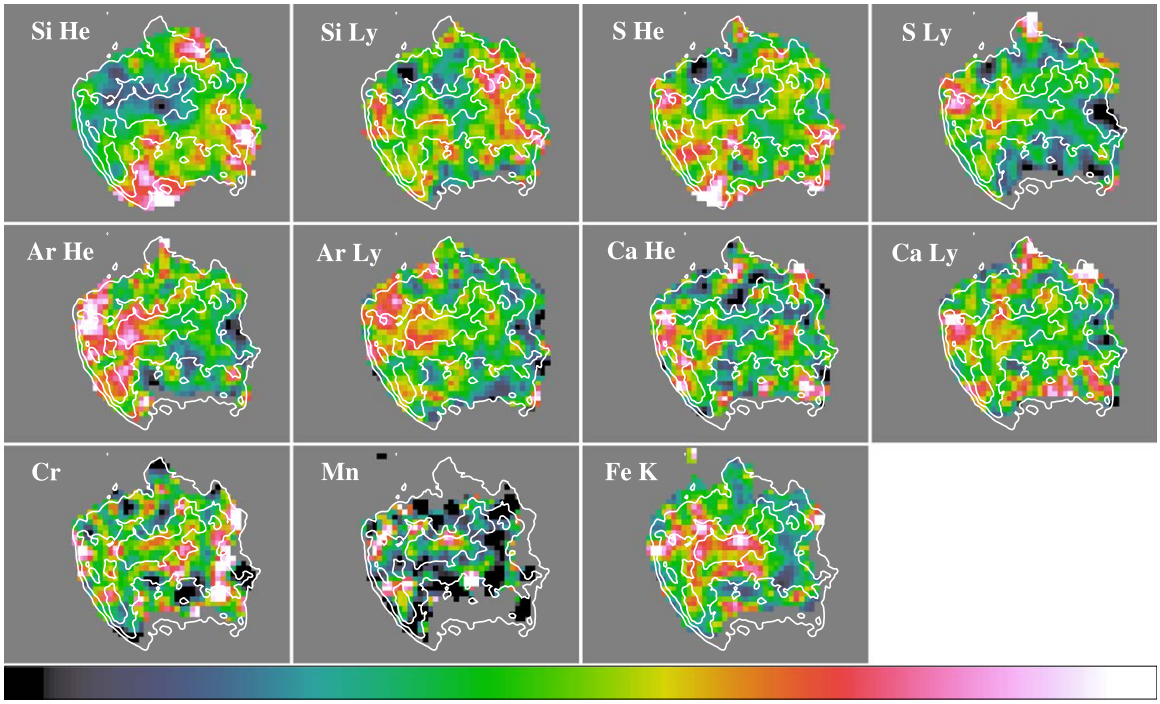

Figure 5. EW maps of emission lines. The EW range between 100–300 (Si He); 80–200 (Si Ly), 150–350 (S He), 80–250 (S Ly), 80–200 (Ar He), 0–100 (Ar Ly), 120–240 (Ca He), 0–120 (Ca Ly), 0–120 (Cr), 0–120 (Mn), and 0–8500 (Fe K) in units of eV. The color bar has a linear scale. The white contours denote the Chandra 0.5–8.0 keV flux (Lopez et al. 2013).

periphery of the remnant. This indicates that although the central bar-like structure has the highest emission measure for almost all the emission lines, the true distributions of the metal abundances show stratified features.

4. Discussion

4.1. Density and Mass of the X-Ray-emitting Plasma

Based on the normalization parameters[8] obtained in global spectral fitting, we further estimate the electron densities of the individual plasma component in W49B. Assuming a spherical geometry of the remnant with a radius of $\sim 2\farcs2$, the electron densities are obtained as $n_{\rm e,1} = 0.46 \pm 0.01 f_1^{-0.5} d_{9.3}^{-0.5}\,{\rm cm}^{-3}$, $n_{\rm e,2} = 0.62 \pm 0.01 f_2^{-0.5} d_{9.3}^{-0.5}\,{\rm cm}^{-3}$, and $n_{\rm e,3} = 18.17 \pm 0.06 f_3^{-0.5} d_{9.3}^{-0.5}\,{\rm cm}^{-3}$ (hereafter, we use the subscripts 1, 2, and 3 to indicate the parameters related to the high-temperature RP, the low-temperature RP, and the CIE component, respectively), where $d_{9.3} = d/(9.3\ {\rm kpc})$ is the distance scaled to 9.3 kpc. If we further assume that the three plasma components are in pressure balance (i.e., $n_{\rm e,1}kT_{\rm e,1} = n_{\rm e,2}kT_{\rm e,2} = n_{\rm e,3}kT_{\rm e,3}$) and sharing the whole volume (i.e., $f_1 + f_2 + f_3 = 1$), the densities and filling factors can be calculated as $n_{\rm e,1} = 2.1 \pm 0.1 d_{9.3}^{-0.5}\,{\rm cm}^{-3}$, $n_{\rm e,2} = 5.2 \pm 0.3 d_{9.3}^{-0.5}\,{\rm cm}^{-3}$, $n_{\rm e,3} = 18.8 \pm 0.1 d_{9.3}^{-0.5}\,{\rm cm}^{-3}$ and $f_1 \sim 5.0\%$, $f_2 \sim 1.4\%$, and $f_3 \sim 93.6\%$, respectively. The parameters obtained above indicate that the X-ray emitting volume in W49B is dominated by the shocked ISM, while the metal-rich RP components distribute in a rather small part of the remnant (with a total filling factor of $<10\%$). The total masses of the X-ray emitting gas are $M_1 = 2.7 \pm 0.4 d_{9.3}^{2.5}\,M_\odot$, $M_2 = 1.9 \pm 0.3 d_{9.3}^{2.5}\,M_\odot$, and $M_3 = 452 \pm 5 d_{9.3}^{2.5}\,M_\odot$.

Kawasaki et al. (2005) constrained the masses of the high- and low-temperature plasma in W49B to be $M_{\rm HT} \sim 34 d_{9.3}^{2.5}\,M_\odot$ and $M_{\rm LT} \sim 138 d_{9.3}^{2.5}\,M_\odot$, respectively, based on Chandra observations. Recently, Zhou & Vink (2018) carried out a spatially resolved spectroscopic study of W49B, and obtained the gas masses as $M_{\rm HT} \sim 43 d_{9.3}^{2.5}\,M_\odot$ and $M_{\rm LT} \sim 404 d_{9.3}^{2.5}\,M_\odot$. We note that the above works suggested a much higher mass for the high-temperature, ejecta-dominated plasma than that we obtained here ($M_1 + M_2 \sim 4.6 d_{9.3}^{2.5}\,M_\odot$). We consider this as a result of the different spectral models adopted in different works. As analyzed in Section 3.1, the global spectra of W49B are best characterized by a three-temperature plasma model ($kT_{\rm e,1} \sim 1.60$ keV, $kT_{\rm e,2} \sim 0.64$ keV, $kT_{\rm e,3} \sim 0.18$ keV), while both of the above works used a two-temperature model to fit the spectra ($kT_{\rm e,HT} \sim 0.6$–2.2 keV, and $kT_{\rm e,LT} \sim 0.27$ keV). As a result, the electron temperature of the cold ISM-dominated component may be overestimated, while the normalization may be underestimated in these works. Our analysis reveals a rather large normalization parameter for the low-temperature ISM, which is more than two orders of magnitude higher than that of the shocked ejecta. This then naturally results in a rather small filling factor and gas mass of the ejecta-dominated plasma according to the calculations above.

4.2. Ionization Temperature

The ionization temperature (kT_z) is commonly used to describe the ionization state of the plasma. It can be estimated by the flux ratios between H-like and He-like emission lines (e.g., Kawasaki et al. 2002; Ozawa et al. 2009; Lopez et al. 2013), but may vary from one ion species to another. Here, we

[8] Defined as $10^{-14}/(4\pi d^2)\int n_{\rm e} n_{\rm H} f dV$, where d is the distance to the remnant, $n_{\rm e}$ and $n_{\rm H}$ are the electron and hydrogen density, and f is the filling factor; $n_{\rm e} = 1.2 n_{\rm H}$ for a fully ionized plasma with solar abundance.

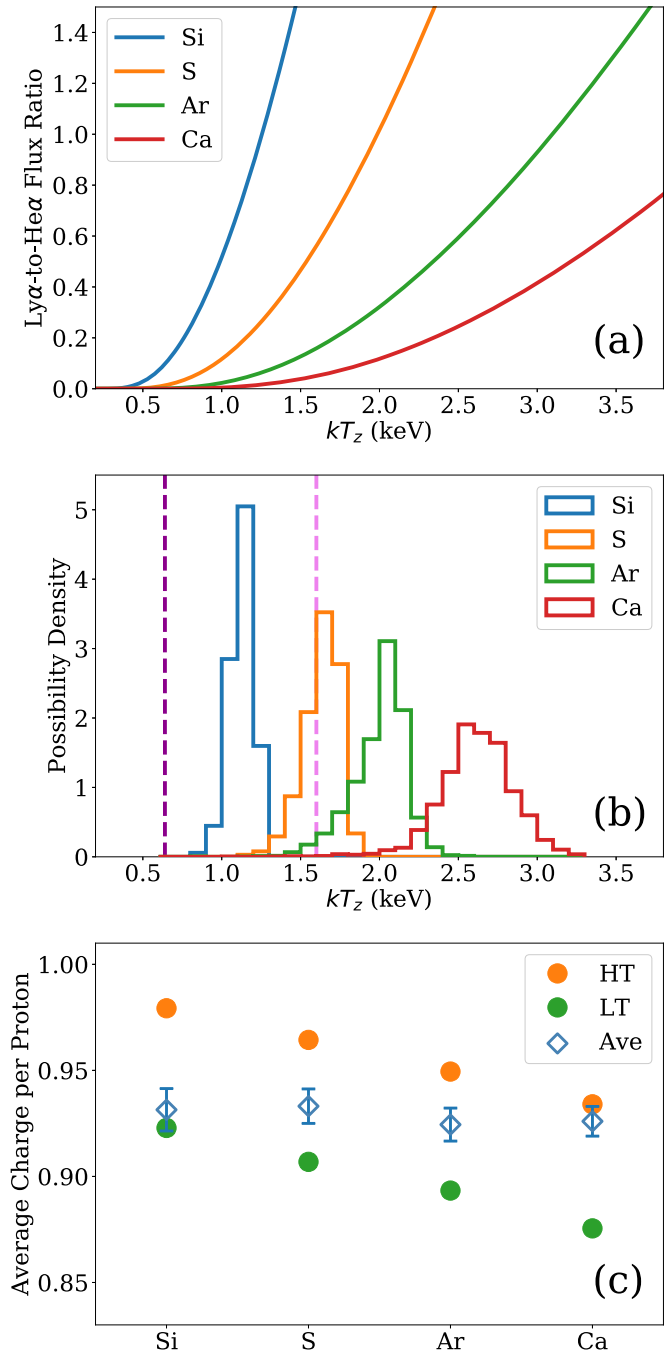

Figure 6. (a) The modeled relations between the Lyα-to-Heα flux ratios and kT_z; (b) the flux-weighted possibility distribution functions of the kT_z for Si, S, Ar, and Ca, the dark and light magenta dashed lines indicate the kT_e of two RP components ($\sim$0.64 and $\sim$1.6 keV), respectively; (c) the average charges of Si, S, Ar, and Ca calculated from the flux ratios, compared with those calculated from the best-fit parameters of the HT and the LT RP components obtained in Section 3.1.

estimate the ionization temperatures for Si, S, Ar, and Ca based on their Lyα and Heα line flux obtained in Section 3.2. The modeled relations between the Lyα-to-Heα flux ratios and kT_z are shown in Figure 6(a), which are derived from the SPEX code[9] (Kaastra et al. 1996). With these relations, we estimate the ionization temperatures and their distributions in W49B, as shown in Figure 7.

[9] https://www.sron.nl/astrophysics-spex

We further calculate the flux-weighted possibility distribution functions of the kT_z for different ion species based on their line flux and kT_z maps, as shown in Figure 6(b). We find that the average ionization temperatures of different ion species are indeed different: $\overline{kT}_{z,Si} = 1.13 \pm 0.08$ for Si, $\overline{kT}_{z,S} = 1.63 \pm 0.12$ for S, $\overline{kT}_{z,Ar} = 2.00 \pm 0.17$ for Ar, and $\overline{kT}_{z,Ca} = 2.62 \pm 0.25$ for Ca (here, we give the flux-weighted averages and their standard deviations). Additionally, the overionization states of Si, S, Ar, and Ca can be further evidenced by comparing their average ionization temperatures with the electron temperatures obtained before $kT_{e,1} \approx 1.60$ keV and $kT_{e,2} \approx 0.64$ keV. Lopez et al. (2013) analyzed the Chandra spectra of 13 regions in W49B, and obtained the ionization temperatures of S and Ar as $\overline{kT}_{z,S} \approx 1.3$–$1.7$ keV and $\overline{kT}_{z,Ar} \approx 1.5$–$2.1$ keV, which are consistent with the results of this work.

The difference of kT_z among ion species may result from the different initial conditions and recombination history (e.g., Sawada & Koyama 2012). In the case of W49B, we find that the kT_z of Si and S are lower than those of Ar and Ca. This seems to be unphysical for a single temperature RP, given that the recombination timescales of Si and S are longer than those of Ar and Ca under a temperature of $\sim 10^7$ K (Smith & Hughes 2010), as pointed out by Lopez et al. (2013). However, it has been shown that the RP in W49B consists of at least two major components with different temperatures and ionization parameters (Section 3.1). Thus the difference of kT_z can be reasonably understood as a result of the different distributions of ion populations among different RP components. Figure 6(c) shows the average charges of different ion species calculated with the SPEX code, using the flux-ratio-inferred average kT_z obtained above, and the best-fit parameters (i.e., electron temperatures and ionization parameters) of the two RP components obtained in Section 3.1, respectively. We find that the flux-ratio-inferred and spectral-fitting-inferred average charges consist well with each other, which strengthens the reliability of both approaches. Moreover, Figure 6(c) indicates that Si and S are dominated in the low-temperature RP while Ar and Ca are dominated in the high-temperature RP, which may be responsible for a lower kT_z of Si and S.

4.3. Recombination Age and the Origin of the RP

With the electron density n_e and the ionization parameter $n_e t$ given, we can estimate the elapsed time since the RP was formed, which is the so-called recombination age (t_{rec}). At a distance of 9.3 kpc, the recombination ages are derived as $t_{rec,1} = 6000 \pm 400$ yr for the high-temperature RP and $t_{rec,2} = 3400 \pm 200$ yr for the low-temperature RP, respectively. As a comparison, Zhou & Vink (2018) obtained similar results with $t_{rec} \sim$ 2000–6000 yr, based on Chandra observations.

The physical origin of the RP presented in SNRs has not been clearly understood. As mentioned above, there are two major scenarios that may lead to rapid electron cooling and result in overionization: adiabatic expansion (e.g., Itoh & Masai 1989) and thermal conduction (e.g., Kawasaki et al. 2002; Zhou et al. 2011). In the case of W49B, there is already some observational evidence for a gradient of increasing overionization degree from east to west, which supports an adiabatic expansion origin of RP (e.g., Miceli et al. 2010; Lopez et al. 2013; Yamaguchi et al. 2018). On the other hand, the thermal conduction between ambient clouds and hot plasma may also play an important role in forming the RP, as revealed by Zhou et al. (2011) and Zhang et al. (2019) based on

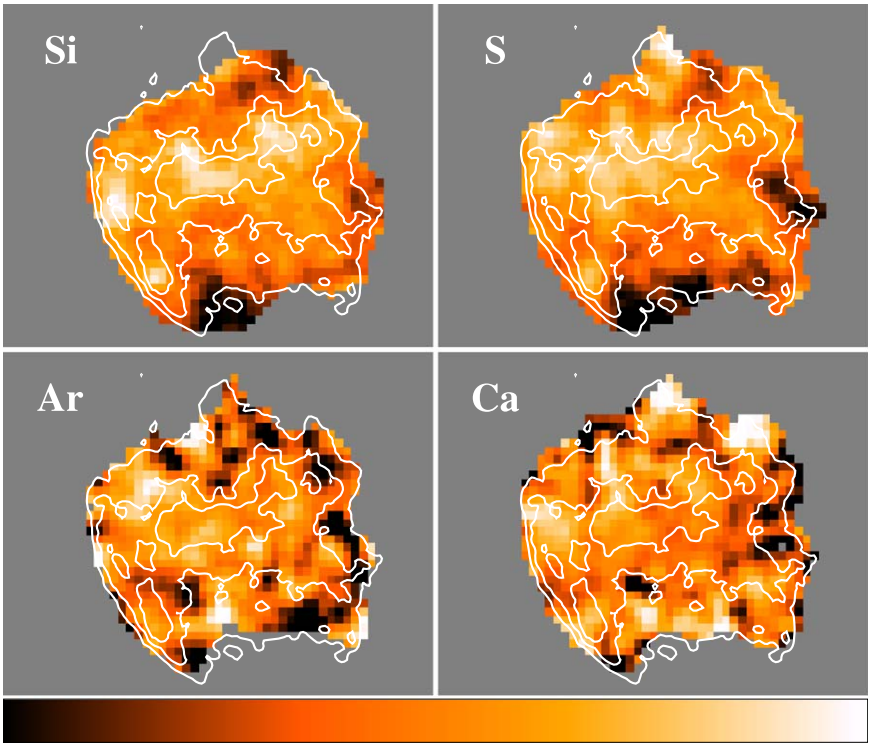

Figure 7. Distribution maps of kT_z for Si, S, Ar, and Ca in W49B. kT_z range between 0.9–1.3 keV for Si, 1.3–1.9 keV for S, 1.6–2.4 keV for Ar, and 2.0–3.2 keV for Ca. The color bar has a linear scale.

hydrodynamic simulations. Observationally, one can investigate the possibility of the thermal conduction origin of RP by comparing the conduction timescale $t_{\rm cond}$ with the recombination age $t_{\rm rec}$ (e.g., Kawasaki et al. 2002; Uchida et al. 2012; Sato et al. 2014). The classical conduction timescale can be estimated as

$$t_{\rm cond} \approx 2 \times 10^{10} \left(\frac{n_{\rm e}}{1\ {\rm cm}^{-3}}\right)\left(\frac{l_{\rm T}}{1\ {\rm pc}}\right)^2\left(\frac{kT_{\rm e}}{1.0\ {\rm keV}}\right)^{-5/2}\left(\frac{\ln\Lambda}{32.2}\right) {\rm s}, \quad (2)$$

where $l_{\rm T} \equiv ({\rm grad}\ln T)^{-1}$ is the temperature gradient scale length and $\ln\Lambda$ is the Coulomb logarithm (Spitzer 1962; Kawasaki et al. 2002; Zhou et al. 2014). For the high-temperature RP component with an initial temperature $kT_{\rm init,1} \sim 4.5$ keV and an electron density $n_{\rm e,1} \sim 2.1\,{\rm cm}^{-3}$, it can efficiently cool down by thermal conduction in a timescale of $t_{\rm cond,1} \sim 1100\ {\rm yr} < t_{\rm rec,1}$. But for the low-temperature RP component with $kT_{\rm init,2} \sim 2.4$ keV and $n_{\rm e,2} \sim 5.2\,{\rm cm}^{-3}$, the timescale is $t_{\rm cond,2} \sim 13,000\ {\rm yr} > t_{\rm rec,2}$. Here, we assume $l_{\rm T} \sim 6$ pc, which is comparable with the SNR radius. Therefore, the thermal conduction scenario is a possible origin for the high-temperature RP in W49B, while it may not apply to the low-temperature RP due to a much longer cooling timescale. If the thermal conduction takes place on a smaller scale, where the temperature gradient scale length $l_{\rm T}$ is comparable or even shorter than the electron mean free path $\lambda_{\rm e} \approx 0.4(kT_{\rm e}/1.0\ {\rm keV})^2(n_{\rm e}/1\ {\rm cm}^{-3})^{-1}$ pc, the heat flux becomes saturated (Cowie & McKee 1977). However, the hydrodynamic simulations which include the effect of saturated thermal conduction show that the conduction timescale can still be a few $\times 10^3$ yr (e.g., Zhou et al. 2011), and thus has little effect on our conclusions here.

Actually, the adiabatic expansion and the thermal conduction may simultaneously contribute to the formation of the RP, especially when the SNR associates with a complex cloud environment, such as in the case of W49B (e.g., Zhou et al. 2011; Zhang et al. 2019).

4.4. SN Type of W49B

The SN type of W49B is still under debate. It is usually considered as a remnant of CC SN, based on its unique morphology and environment, the metal abundances, and the Fe K line centroid (e.g., Miceli et al. 2006; Keohane et al. 2007; Lopez et al. 2013; Yamaguchi et al. 2014). Moreover, the progenitor seems to be a supermassive star ($\gtrsim 25\,M_\odot$) which produced a black hole rather than a neutron star (NS; Lopez et al. 2013). However, the rather small cavity size (radius ~5–7 pc, see, e.g., Keohane et al. 2007; Chen et al. 2014) disfavors a supermassive progenitor. On the other hand, the CC origin has been recently doubted by Zhou & Vink (2018), who pointed out that the metal abundances are better described by SN Ia models.

In Figure 8, we compare the metal abundance ratios of the ejecta in W49B with the predicted results of different SN nucleosynthesis models. Based on the spectral fitting results, the abundance ratios of the RP components are obtained as Si/Fe = 0.74 ± 0.01, S/Fe = 1.01 ± 0.01, Ar/Fe = 1.12 ± 0.02, Ca/Fe = 1.14 ± 0.02, Cr/Fe = 1.32 ± 0.11, and Mn/Fe = 1.89 ± 0.22. The SN models considered here include normal CC SN and energetic hypernova models with different stellar masses and explosion energies (Nomoto et al. 2006); typical spherical CC SN models with different stellar masses (Sukhbold et al. 2016); a 1D deflagration SN Ia model W7 and 2D delayed-detonation (DDT)

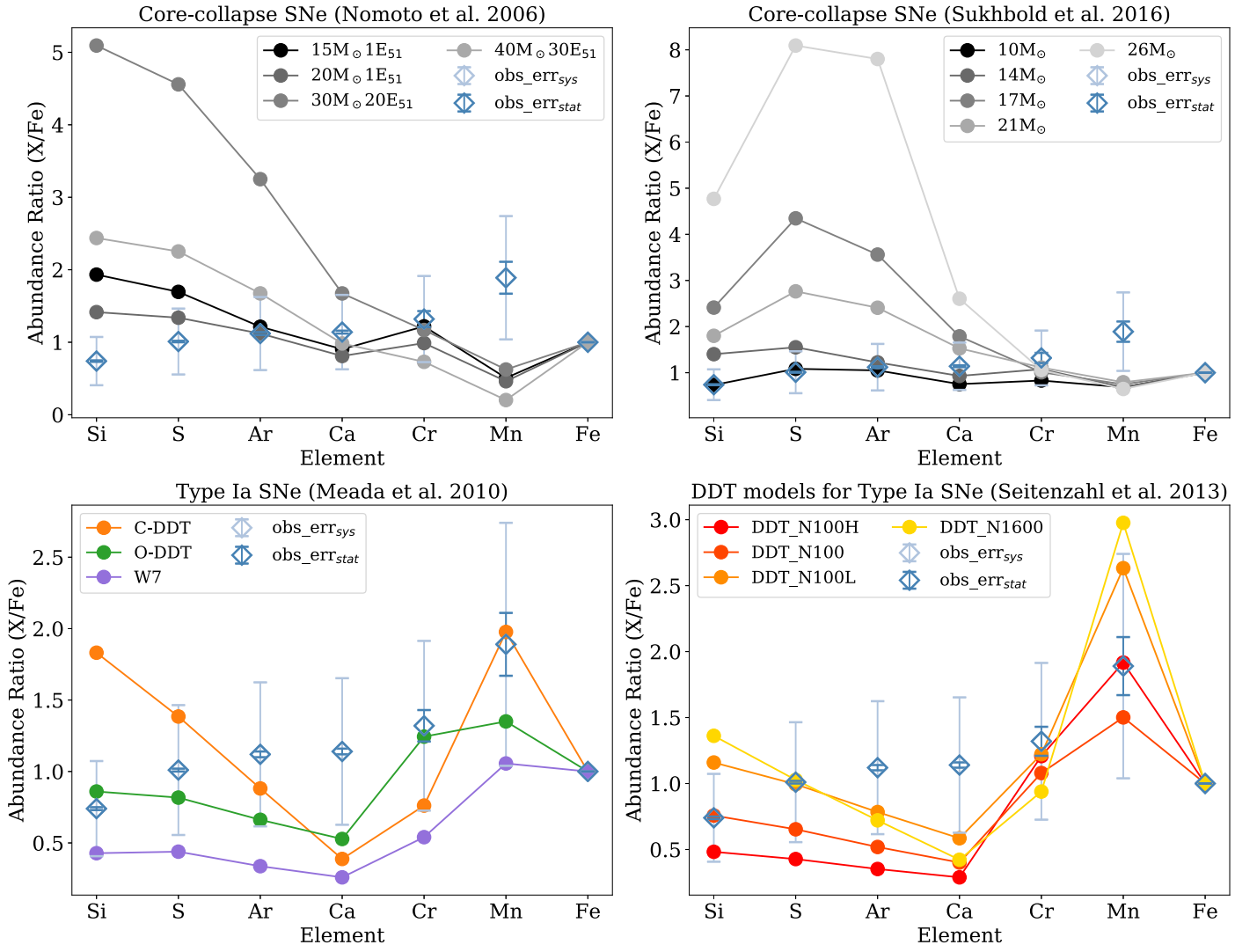

Figure 8. Metal abundance ratios of W49B (empty diamonds; the error bars in dark blue indicate the statistical errors, while those in light blue indicate the systematic errors), compared with the predicted results of different SN nucleosynthesis models (filled circles). Refer to the text for a detailed description of the SN models.

SN Ia models with center/off-center ignition (Maeda et al. 2010); and 3D DDT SN Ia models with different multispot ignition setups (Seitenzahl et al. 2013). We find that neither CC SN models nor SN Ia models can perfectly reproduce the observations. The abundances of the IMEs such as Si, S, Ar, and Ca favor a CC explosion, and can be well described by 10–14 $M_\odot$ progenitor models. But none of the CC SN models can reproduce the Mn-to-Fe abundance ratio as high as the observation. On the other hand, some of the SN Ia models such like the multispot ignited 3D DDT models (Seitenzahl et al. 2013) may explain the high Cr and Mn abundances, while they systematically underestimate the abundances of Ar and Ca.

We then turn to comparing the observed masses of different metal species in ejecta with the model predicted results. The metal masses are derived from the total ejecta mass and the abundances as $M_{\rm Si} = (2.3 \pm 0.3) \times 10^{-2}\,M_\odot$, $M_{\rm S} = (1.4 \pm 0.2) \times 10^{-2}\,M_\odot$, $M_{\rm Ar} = (3.4 \pm 0.4) \times 10^{-3}\,M_\odot$, $M_{\rm Ca} = (3.3 \pm 0.4) \times 10^{-3}\,M_\odot$, $M_{\rm Cr} = (1.0 \pm 0.2) \times 10^{-3}\,M_\odot$, $M_{\rm Mn} = (0.9 \pm 0.2) \times 10^{-3}\,M_\odot$, and $M_{\rm Fe} = (6.0 \pm 0.6) \times 10^{-2}\,M_\odot$. We note that only the X-ray emitting gas mass is counted here, which is potentially lower than the total mass produced by SN explosion. As shown in Figure 9, the observed metal masses are basically consistent with the yields of CC SN models and indicate a progenitor mass of 10–14 $M_\odot$. However, the Mn mass is higher than the predicted values of all the CC SN models, with a factor of 2–5. SN Ia models produce much more metals than observations, for all the species considered here. If we multiply the observed masses by a factor of 10 (the gray data points in Figure 9), they would get close to the yields in the SN Ia models, except for Ar and Ca.

As a conclusion, we have not found an SN model that can properly describe all the observational features. The progenitor of W49B remains unclear. However, our results provide new implications and constraints on it, which are described below.

1. If we consider W49B as a CC SNR, the analysis above indicates that the progenitor is more likely a $\lesssim$15 $M_\odot$ star rather than a supermassive star suggested by Lopez et al. (2013). A relatively small progenitor mass ($\sim$13 $M_\odot$) is also indicated by the small cavity size (Chen et al. 2014). In addition, nucleosynthesis in energetic explosions of the supermassive stars is characterized by smaller (Cr, Mn)/Fe than normal SNe (e.g., Nomoto et al. 2006), which disagrees with what we have found in W49B. However, an unusually high abundance of Mn in W49B is hard to understand in a CC scenario. In CC SNe, Mn is mainly produced in incomplete explosive Si-burning conditions.

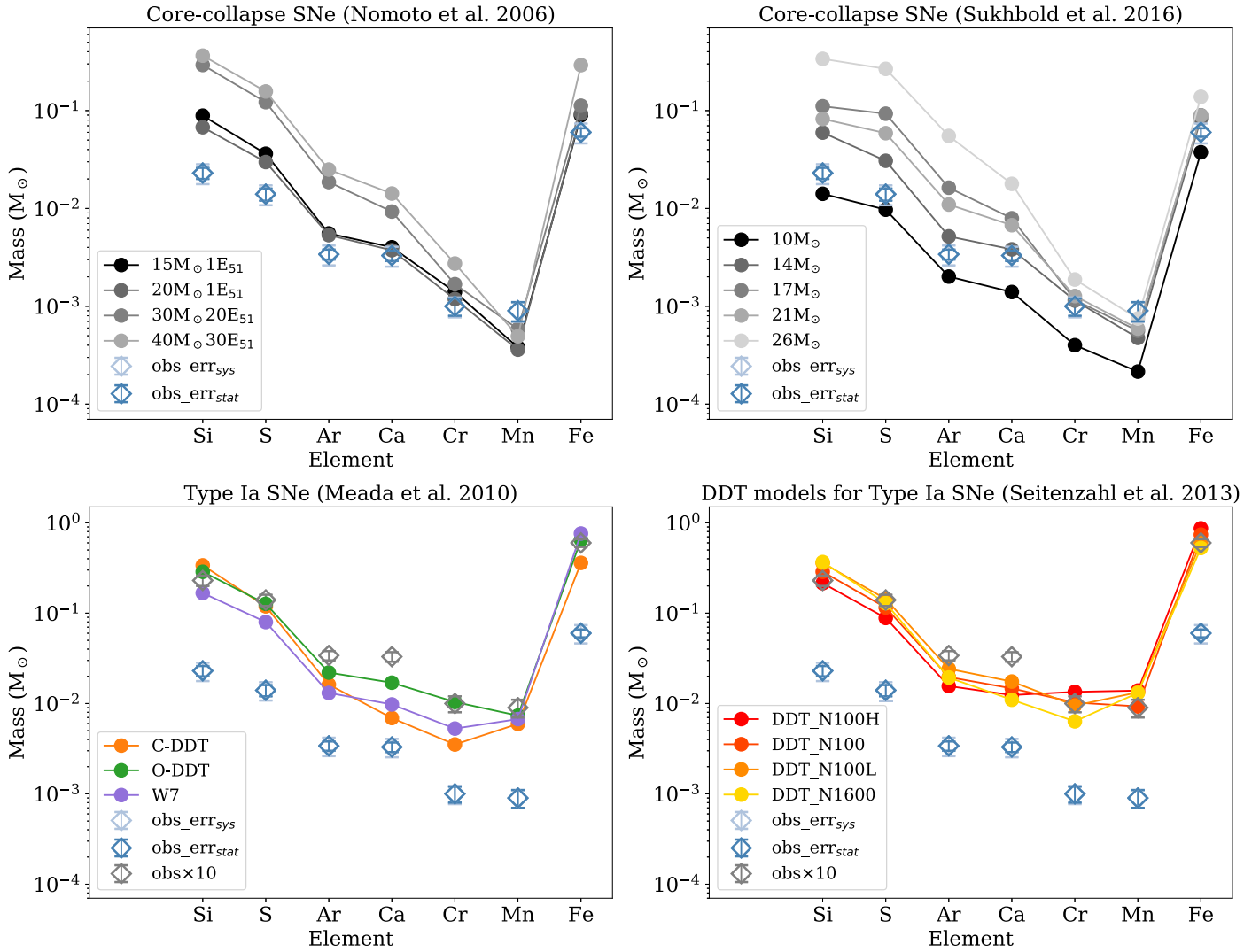

Figure 9. Similar to Figure 8, but the metal masses of the shocked ejecta in W49B.

Mn yield and the final Mn/Fe ratio increase with the increasing initial metallicity of the progenitor, and may be affected by detailed explosion mechanisms (see, e.g., Nomoto et al. 2013; Thielemann et al. 2018, for recent reviews on SN nucleosynthesis). However, it seems unlikely to have Mn/Fe > 1 according to existing CC SN models. Another problem for the CC scenario is the undetected stellar remnant. The SN explosion of a $\lesssim$15 $M_\odot$ star will leave a newborn NS, which radiates X-ray emission, while no detection of such a source has been confirmed yet. Recently, Zhou & Vink (2018) reported the detection of 24 point-like X-ray sources in the vicinity of W49B and found that nine of them are in the luminosity range predicted for an NS at an age of 5–6 kyr according to the modeled cooling curve. Therefore, they suggested there is still the possibility that W49B harbors a cooling NS.

2. If we consider W49B as an Ia SNR, the metal abundances we obtained above favor a DDT explosion with multispot ignition. The relatively small metal masses indicate that the X-ray emitting ejecta in W49B only account for ~10% of the total SN ejecta. The rest of the ejecta may remain unshocked, or not be hot enough to emit X-ray. Zhu et al. (2014) found two dust components associated with W49B based on infrared observations, including a hot component ~150 K and a warm component ~45 K. The masses of the two dust components are estimated as $(7.5 \pm 6.6) \times 10^{-4}\,M_\odot$ and $6.4 \pm 3.2\,M_\odot$, respectively. However, the origins of the dust are suggested to be the swept up circumstellar or interstellar materials and the evaporation of the clouds interacting with W49B, rather than the SN ejecta (Zhu et al. 2014).

We note that the statistical errors of the metal abundances obtained by spectral fitting are very small (see Table 4). In this case, the systematic errors may be more important, which have not been considered above. The systematic errors of the fitting results may originate from multiple aspects, such as the plasma code, the atomic database, and the fitting technique, which make it very difficult to tightly constrain the errors (see, e.g., Hitomi Collaboration et al. 2018, for a detailed discussion). A recent study carried out by Mernier et al. (2019) compared the SPEXACT v3.0.5 (`cie` model) with the AtomDB v3.0.9 (`vapec` model) and indicated systematic differences up to ~20% for the Fe abundance and up to ~45% for the O/Fe, Mg/Fe, Si/Fe, and S/Fe ratios. Therefore, we simply adopt a 20% systematic error for all the metal abundances and a 45% systematic error for all the abundance ratios considered in this

work (see the light blue error bars in Figures 8 and 9), and find that it can barely alter the conclusions obtained above.

5. Summary

We perform a comprehensive X-ray spectroscopy and imaging analysis of SNR W49B using archival XMM-Newton data. We find spectral evidence of overionization in the ejecta-dominated hot plasma not only for Fe, but also for the lighter elements such as Si, S, and Ca. The thermal and ionization properties of the RP are well constrained, which provide new implications for the RP origin and the SN progenitor. The detailed results are summarized as follows.

1. The overionization state of the shocked ejecta in W49B is clearly indicated by the spectral features of (1) RRCs of H-like Si, He-like S, and He-like Fe; (2) Lyα lines of Ca and Fe. We find that the RP has a multitemperature composition, and the global spectra of the remnant can be well reproduced by a "CIE + 2 RP" model. The two RP components are characterized by different electron temperatures and ionization parameters as $kT_{\rm e,1} = 1.60^{+0.02}_{-0.01}$ keV, $n_{\rm e,1}t_1 = 3.90^{+0.08}_{-0.04} \times 10^{11}\,{\rm cm^{-3}\,s}$; and $kT_{\rm e,2} = 0.64 \pm 0.01$ keV, $n_{\rm e,2}t_2 = 5.49^{+0.04}_{-0.09} \times 10^{11}\,{\rm cm^{-3}\,s}$, respectively.
2. We construct the line flux images and the EW maps of various emission lines for W49B. The results indicate that the central bar-like structure has the highest emission measure for almost all the emission lines, while the distributions of metal abundances show clear stratified features: the IMEs like Si and S distribute mainly in the outer regions, while the IGEs like Fe and Mn concentrate mainly in the inner part.
3. The X-ray emitting volume in W49B is dominated by the shocked ISM, while the ejecta-dominated RP components distribute in a rather small part of the remnant (with a total filling factor <10%). The total masses of the X-ray emitting gas are $2.7 \pm 0.4 d_{9.3}^{2.5}\,M_\odot$, $1.9 \pm 0.3 d_{9.3}^{2.5}\,M_\odot$, and $452 \pm 5 d_{9.3}^{2.5}\,M_\odot$ for the two RP components and the shocked ISM, respectively.
4. Based on the Lyα-to-Heα flux ratios, we estimate the average ionization temperatures of Si, S, Ar, and Ca as $\overline{kT}_{\rm z,Si} = 1.13 \pm 0.08$, $\overline{kT}_{\rm z,S} = 1.63 \pm 0.12$, $\overline{kT}_{\rm z,Ar} = 2.00 \pm 0.17$, and $\overline{kT}_{\rm z,Ca} = 2.62 \pm 0.25$. Combined with the electron temperatures obtained above ($kT_{\rm e,1} \sim 1.60$ keV and $kT_{\rm e,2} \sim 0.64$ keV), the ionization temperatures provide further evidence of the overionization. The difference of $kT_{\rm z}$ among ion species may result from the different initial conditions and recombination history, and from the different distributions of ion populations among different RP components.
5. We obtain the recombination ages 6000 ± 400 yr for the high-temperature RP and 3400 ± 200 yr for the low-temperature RP, respectively. On the other hand, the thermal conduction timescales of the two RP components are derived to be ~1100 yr and ~13,000 yr, respectively. This indicates that the thermal conduction scenario is a possible origin for the high-temperature RP in W49B, while it may not apply to the low-temperature component. Following recent results of the hydrodynamic simulations, we suggest that different scenarios such as the adiabatic expansion and the thermal conduction may simultaneously contribute to the formation of the RP in W49B.
6. Although the metal abundances and masses cannot be perfectly characterized by existing SN models, they provide new implications and constraints on the progenitor of W49B. If W49B originates from a CC explosion, our results suggest the progenitor mass to be $\lesssim 15\,M_\odot$. But the high Mn abundance (Mn/Fe > 1) will be confusing in the CC context. If W49B originates from an SN Ia, our results indicate that the metal abundance ratios could be roughly consistent with a DDT model with multispot ignition, but the X-ray emitting ejecta only account for ~10% of the total SN ejecta.

We thank Ping Zhou and Gao-Yuan Zhang for the valuable discussions. This work is supported by National Key R&D Program of China No. 2017YFA0402600 and the NSFC under grants 11773014, 11633007, and 11851305. L.S. acknowledges the financial support of the China Scholar Council (No. 201906190108).

Software: XSPEC (Arnaud 1996), SPEX (Kaastra et al. 1996), SAS, DS9.[10]

ORCID iDs

Lei Sun (孫磊) https://orcid.org/0000-0001-9671-905X
Yang Chen (陳陽) https://orcid.org/0000-0002-4753-2798

References

Arnaud, K. A. 1996, in ASP Conf. Ser. 101, Astronomical Data Analysis Software and Systems V, ed. G. H. Jacoby & J. Barnes (San Francisco, CA: ASP), 17
Auchettl, K., Ng, C.-Y., Wong, B. T. T., Lopez, L., & Slane, P. 2017, ApJ, 847, 121
Auchettl, K., Slane, P., Castro, D., Foster, A. R., & Smith, R. K. 2015, ApJ, 810, 43
Broersen, S., & Vink, J. 2015, MNRAS, 446, 3885
Chen, Y., Jiang, B., Zhou, P., et al. 2014, in IAU Symp. 296, Supernova Environmental Impacts, ed. A. Ray & R. A. McCray (Cambridge: Cambridge Univ. Press), 170
Cowie, L. L., & McKee, C. F. 1977, ApJ, 211, 135
Ergin, T., Sezer, A., Saha, L., et al. 2014, ApJ, 790, 65
Ergin, T., Sezer, A., Sano, H., Yamazaki, R., & Fukui, Y. 2017, ApJ, 842, 22
Ferrand, G., & Safi-Harb, S. 2012, AdSpR, 49, 1313
Greco, E., Miceli, M., Orlando, S., et al. 2018, A&A, 615, A157
H.E.S.S. Collaboration, Abdalla, H., Abramowski, A., et al. 2018, A&A, 612, A5
Hitomi Collaboration, Aharonian, F., Akamatsu, H., et al. 2018, PASJ, 70, 12
Hwang, U., Holt, S. S., & Petre, R. 2000, ApJL, 537, L119
Hwang, U., Petre, R., & Hughes, J. P. 2000, ApJ, 532, 970
Itoh, H., & Masai, K. 1989, MNRAS, 236, 885
Jiang, B., Chen, Y., Wang, J., et al. 2010, ApJ, 712, 1147
Kaastra, J. S., Mewe, R., & Nieuwenhuijzen, H. 1996, in 11th Coll. on UV and X-ray Spectroscopy of Astrophysical and Laboratory Plasmas, ed. K. Yamashita & T. Watanabe (Tokyo: Universal Academy Press), 411
Kamitsukasa, F., Koyama, K., Uchida, H., et al. 2015, PASJ, 67, 16
Katayama, H., Takahashi, I., Ikebe, Y., et al. 2004, A&A, 414, 767
Katsuragawa, M., Nakashima, S., Matsumura, H., et al. 2018, PASJ, 70, 110
Kawasaki, M., Ozaki, M., Nagase, F., et al. 2005, ApJ, 631, 935
Kawasaki, M. T., Ozaki, M., Nagase, F., et al. 2002, ApJ, 572, 897
Keohane, J. W., Reach, W. T., Rho, J., et al. 2007, ApJ, 654, 938
Kuntz, K. D., & Snowden, S. L. 2008, A&A, 478, 575
Lopez, L. A., Pearson, S., Ramirez-Ruiz, E., et al. 2013, ApJ, 777, 145
Lopez, L. A., Ramirez-Ruiz, E., Badenes, C., et al. 2009, ApJL, 706, L106
Lopez, L. A., Ramirez-Ruiz, E., Castro, D., & Pearson, S. 2013, ApJ, 764, 50
Lopez, L. A., Ramirez-Ruiz, E., Huppenkothen, D., et al. 2011, ApJ, 732, 114
Maeda, K., Röpke, F. K., Fink, M., et al. 2010, ApJ, 712, 624
Masui, K., Mitsuda, K., Yamasaki, N. Y., et al. 2009, PASJ, 61, S115
Matsumura, H., Tanaka, T., Uchida, H., Okon, H., & Tsuru, T. G. 2017, ApJ, 851, 73

[10] http://ds9.si.edu/site/Home.html

Matsumura, H., Uchida, H., Tanaka, T., et al. 2017, PASJ, 69, 30
Mernier, F., Werner, N., Lakhchaura, K., et al. 2019, AN, 341, 203
Miceli, M., Bocchino, F., Decourchelle, A., Ballet, J., & Reale, F. 2010, A&A, 514, L2
Miceli, M., Decourchelle, A., Ballet, J., et al. 2006, A&A, 453, 567
Moffett, D. A., & Reynolds, S. P. 1994, ApJ, 437, 705
Nomoto, K., Kobayashi, C., & Tominaga, N. 2013, ARA&A, 51, 457
Nomoto, K., Tominaga, N., Umeda, H., Kobayashi, C., & Maeda, K. 2006, NuPhA, 777, 424
Ohnishi, T., Koyama, K., Tsuru, T. G., et al. 2011, PASJ, 63, 527
Ohnishi, T., Uchida, H., Tsuru, T. G., et al. 2014, ApJ, 784, 74
Okon, H., Uchida, H., Tanaka, T., Matsumura, H., & Tsuru, T. G. 2018, PASJ, 70, 35
Ozawa, M., Koyama, K., Yamaguchi, H., Masai, K., & Tamagawa, T. 2009, ApJL, 706, L71
Pannuti, T. G., Rho, J., Kargaltsev, O., et al. 2017, ApJ, 839, 59
Patnaude, D., & Badenes, C. 2017, in Handbook of Supernovae, ed. A. W. Alsabti & P. Murdin (Berlin: Springer), 2233
Patnaude, D. J., Lee, S.-H., Slane, P. O., et al. 2015, ApJ, 803, 101
Pye, J. P., Becker, R. H., Seward, F. D., et al. 1984, MNRAS, 207, 649
Radhakrishnan, V., Goss, W. M., Murray, J. D., et al. 1972, ApJS, 24, 49
Ranasinghe, S., & Leahy, D. A. 2018, AJ, 155, 204
Rho, J., & Petre, R. 1998, ApJL, 503, L167
Sato, T., Koyama, K., Takahashi, T., Odaka, H., & Nakashima, S. 2014, PASJ, 66, 124
Sawada, M., & Koyama, K. 2012, PASJ, 64, 81
Seitenzahl, I. R., Ciaraldi-Schoolmann, F., Röpke, F. K., et al. 2013, MNRAS, 429, 1156
Sezer, A., Ergin, T., Yamazaki, R., et al. 2019, MNRAS, 489, 4300
Smith, A., Jones, L. R., Peacock, A., et al. 1985, ApJ, 296, 469
Smith, R. K., & Hughes, J. P. 2010, ApJ, 718, 583
Spitzer, L. 1962, Physics of Fully Ionized Gases (New York: Interscience)
Sukhbold, T., Ertl, T., Woosley, S. E., Brown, J. M., & Janka, H.-T. 2016, ApJ, 821, 38
Sun, L., & Chen, Y. 2019, ApJ, 872, 45
Suzuki, H., Bamba, A., Nakazawa, K., et al. 2018, PASJ, 70, 75
Thielemann, F.-K., Isern, J., Perego, A., & von Ballmoos, P. 2018, SSRv, 214, 62
Uchida, H., Koyama, K., Yamaguchi, H., et al. 2012, PASJ, 64, 141
Uchiyama, H., Nobukawa, M., Tsuru, T. G., & Koyama, K. 2013, PASJ, 65, 19
Washino, R., Uchida, H., Nobukawa, M., et al. 2016, PASJ, 68, S4
Yamaguchi, H., Badenes, C., Petre, R., et al. 2014, ApJL, 785, L27
Yamaguchi, H., Ozawa, M., Koyama, K., et al. 2009, ApJL, 705, L6
Yamaguchi, H., Tanaka, T., Wik, D. R., et al. 2018, ApJL, 868, L35
Yamauchi, S., Minami, S., Ota, N., & Koyama, K. 2014, PASJ, 66, 2
Yamauchi, S., Nobukawa, M., Koyama, K., & Yonemori, M. 2013, PASJ, 65, 6
Yang, X. J., Tsunemi, H., Lu, F. J., et al. 2013, ApJ, 766, 44
Zhang, G.-Y., Chen, Y., Su, Y., et al. 2015, ApJ, 799, 103
Zhang, G.-Y., Slavin, J. D., Foster, A., et al. 2019, ApJ, 875, 81
Zhou, P., Safi-Harb, S., Chen, Y., et al. 2014, ApJ, 791, 87
Zhou, P., & Vink, J. 2018, A&A, 615, A150
Zhou, X., Miceli, M., Bocchino, F., Orlando, S., & Chen, Y. 2011, MNRAS, 415, 244
Zhu, H., Tian, W. W., & Zuo, P. 2014, ApJ, 793, 95